GeoStorage

Vol. 1, No. 2, p. 113-124, 2025

Research article

Temperature-treated Sandstone: Mechanical and Failure Behaviour under Triaxial Cyclic Loading

Tao Zhang

School of Civil and Environmental Engineering, Changsha University of Science & Technology, Changsha 410114, China

Keywords:

Numerical simulation
triaxial multi-level cyclic loading
mechanical properties
failure Characteristics
acoustic emission responses

Cited as:

Zhang T. 2025. Temperature-treated Sandstone: Mechanical and Failure Behaviour under Triaxial Cyclic Loading. *GeoStorage*, 1(2), 113-124.
https://doi.org/10.46690/gs.2025.02.02

Abstract:

Understanding thermo-mechanical properties of storage rocks is of great significance for the stability evaluation of underground energy storage projects. In this paper, the particle flow discrete element software (PFC2D) was used to simulate storage sandstone specimens after temperature treatment under triaxial compression and multi-level cyclic loading. Particular attention is paid to the influence of fatigue effect on the mechanical behavior, microcrack propagation, energy evolution, failure mode, and acoustic emission (AE) characteristics of temperature-treated storage sandstone (TTSS) specimens. The comparison of the results of experimental result and numerical simulation demonstrates that the calibrated microscopic parameters are reliable and correct. The results show that the characteristic stresses of the TTSS model, including crack initiation stress, crack damage stress, peak strength, failure strength, and residual strength, increase with increasing confining pressure. The cyclic loading reduces the peak stress of the TTSS model and increases the peak strain. Crack propagation, energy evolution, failure mode, and AE characteristics all depend on the stress level, cyclic loading, and confining pressure. In addition, the fatigue effect increases the number and distribution of microcracks in the TTSS model.

1 Introduction

In the research of compressed air energy storage (CAES) project, nuclear waste disposal project, underground coal gasification, geothermal enhanced thermal extraction, and volcano flank stability, the influence of temperature and complex stress states on the mechanical behavior of rock masses is all involved (Han et al. 2025; Jiang et al. 2020; Liu et al. 2025; Rutqvist et al. 2012; Schmidt et al. 2020; Tunsakul et al. 2013; Yang et al. 2025). For instance, the air pressure and temperature inside the storage cavern are constantly varied throughout the operation of the CAES power station (Fig. 1). The surrounding rock of the storage cavern serves as the main load-bearing structure from temperature and air pressure (Aliyu and Archer 2021; Bouman et al. 2016; Damasceno et al. 2023; Glamheden and Curtis 2006). The accumulation of irreversible plastic deformation of the surrounding rock is caused by the extremely complex thermo-mechanical coupling damage effect. Therefore, it is meaningful for exploring the mechanical properties of the surrounding rock of the storage cavern under coupled temperature-stress.

Hard rocks with high compressive strength and low permeability (like, granite, basalt, limestone, and sandstone) are always chosen as host rocks for underground cave CAES (Perazzelli and Anagnostou 2017; Qin et al. 2023; Xia et al. 2015; Xu et al. 2024b; Zareidarmiyan et al. 2020; Zheng et al. 2024). The mechanical properties and fracture behaviors of rock materials under coupled temperature-stress have received extensive attention (Kim et al. 2012a; Kim et al. 2012b; Kushnir et al. 2012; Xu et al. 2024a). Glover et al. (Glover et al., 1995) monitored the thermal cracking process of quartzite using acoustic emission (AE) technology. The results indicated that the micro-cracking peak (573°C) of quartzite at the phase transformation temperature was detected. Tian et al. (Tian et al., 2019) assessed the evolution of microcracks in granite at different high temperatures using micro-CT. At 200°C, the microcracks propagated in the sample. The microcracks (at 300°C)

Yandy Scientific Press

* Corresponding author.
E-mail address: tzhang_fxk@163.com (Zhang T)

Received Aug. 20, 2025; revised Sep. 18, 2025; accepted Sep. 25, 2025; available online Oct. 5, 2025.

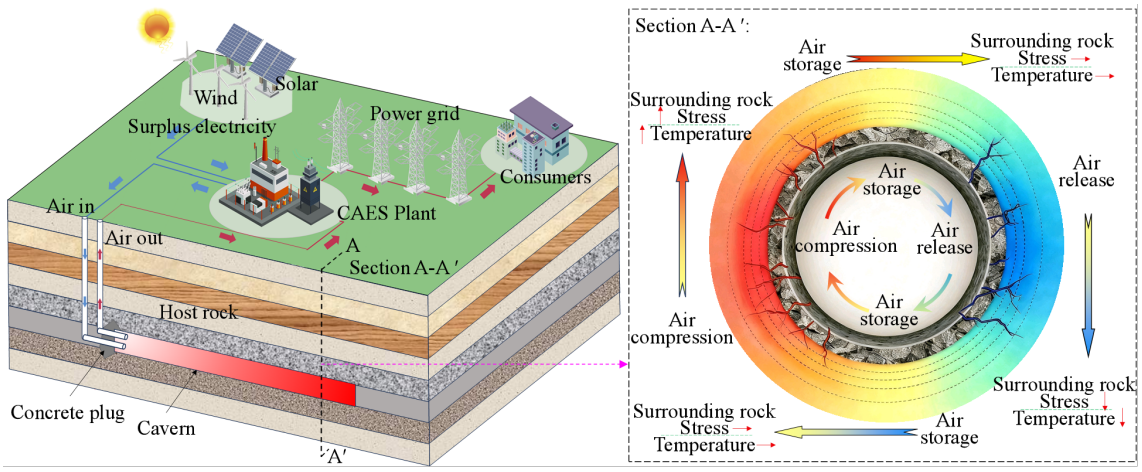

Fig. 1 Three-dimensional diagram of the observation system

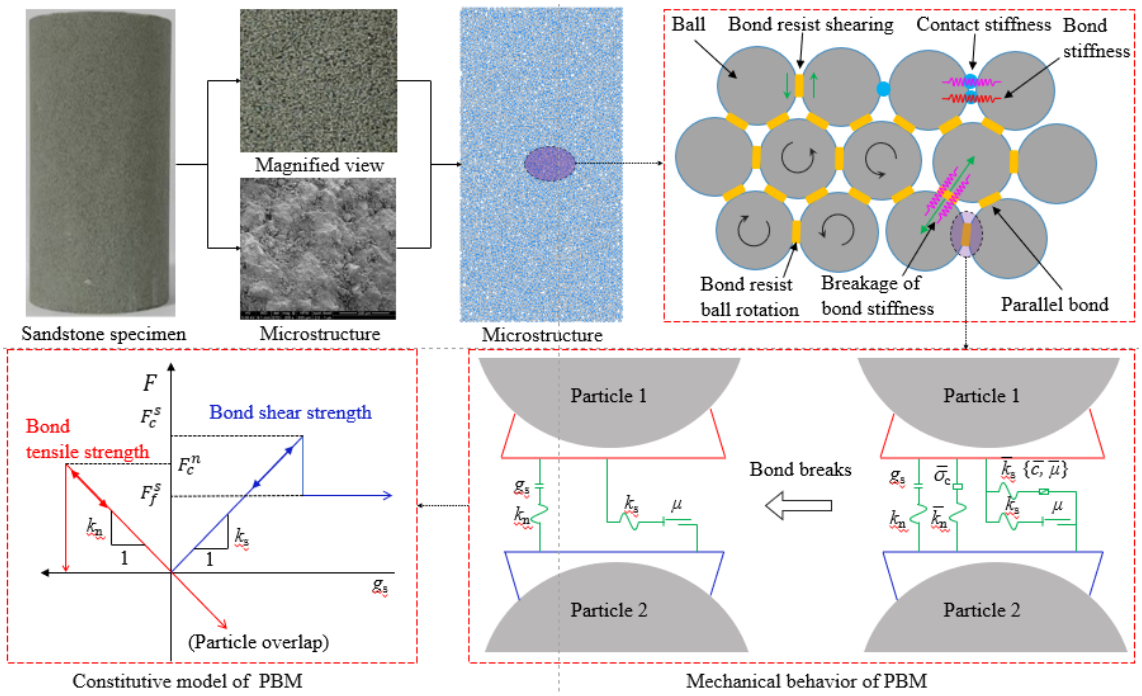

Fig. 2 Establishment of numerical model, mechanical behavior of the PBM, and constitutive model of PBM

gradually developed and even connected to form macrocracks. When the temperature rose to 500°C, the microcrack network formed around the granite grains. Li et al. (Li et al., 2025) investigated the influence of intermediate principal stress on the mechanical behavior of defective granite under thermal cycling. The results showed that at a certain temperature, the strength of rock gradually increased with the increase of intermediate principal stress. However, when the intermediate principal stress reached a certain threshold, the relationship between strength and intermediate principal stress approached a critical state. Meng et al. (Meng et al., 2018) conducted uniaxial mechanical tests of temperature-damaged limestone at different loading rates to explore the evolution of deformation and strength parameters of limestone. The peak strain after failure of limestone increased with the rise of temperature, while the peak stress and elastic modulus of limestone gradually decreased. Zhang et al. (Zhang et al., 2024) investigated the effects of high-temperature treatment and intermediate principal stress on the deformation mechanics and failure behavior of defective granite through true triaxial experiments. Zhou et al. (Zhou et al., 2024) studied the effects of temperature and strain rate on the mechanics behavior of defective sandstone under dynamic loading. The results show that high-temperature treatment strengthened the tensile stress zone and simplified the failure mode. Tian et al. (Tian et al., 2017) analyzed the macroscopic and mesoscopic mechanical behaviors of granite after heat treatment using the cluster model in the particle flow program. Guo et al. (Guo et al., 2023) found that the average peak stress and elastic modulus of granite decreased with the increase of heat treatment temperature, and the average peak strain increased. However, the influence of

temperature and monotonic stress on the mechanical behavior of rock materials has been investigated in the above-mentioned research. The mechanical behavior, energy evolution, and microcrack propagation of storage rocks under temperature and cyclic loading still need to be further reported.

In this work, the temperature treatment process of the storage sandstone was numerically simulated by the PFC2D software. The mechanical behavior, crack propagation, energy evolution, failure mode, and acoustic emission characteristics of the TTSS model under triaxial monotonic and multi-level cyclic loading were further studied and analyzed. The results provide a basis for the subsequent investigation of the mechanical properties of storage rocks under coupled stress-temperature cycling.

2 Modeling procedure

2.1 Numerical model setup

PFC2D, as a commonly used numerical calculation tool, is a two-dimensional particle flow numerical simulation software based on the discrete element method proposed by Cundall and Strack (Cundall and Strack, 1979). In PFC2D, multiple contact models between particles are established to simulate bonding materials, including linear contact bond model, parallel bond model, hertz contact model, and smooth joint model. Matter is mainly composed of particles and bonds. Particles are regarded as rigid particles with tangential and normal stiffness. Bonds are classified into contact keys and parallel keys. Contact bonds can only transfer force. Parallel bonds view the bonds between particles as a set of springs, which can transfer force and momentum between particles. When the particles are bonded, they can resist torque and exhibit linear elasticity. The bonding model is destroyed when the bond strength reaches its maximum value. Therefore, the parallel bond model is more suitable for simulating rock materials.

To realistically simulate laboratory tests, the dimensions of the two-dimensional numerical model are consistent with the specimens of the laboratory test, that is, the width of the model is 50 mm, and the height is 100 mm. The bonding mechanism of the parallel bond model and the detailed information diagram of the numerical model are shown in Fig. 2.

2.2 Determination of micro-parameters

To analyze the mechanical properties and failure characteristics of storage sandstone using the PFC2D numerical simulation software, the micro-parameters must be calibrated and verified to ensure that the numerical simulation is closer to the laboratory test. During this process, the boundary of the numerical simulation is the same as that in the laboratory. The micro-parameters cannot be directly obtained from laboratory test. The micro-parameters are repeatedly adjusted by the "trial and error method", and the results of the numerical simulation are compared with the experimental data from the laboratory test to ensure that the results of the numerical simulation are consistent with the stress-strain curves, peak strength, elastic modulus, and failure mode of the laboratory test. Fig. 3 shows the comparison of the final calibration results of laboratory test and numerical simulation. The mechanical properties of sandstone obtained from laboratory test and numerical simulation are listed in Tab. 1. The results show that the stress-strain curves are similar, and the failure modes are in good agreement. The deviation of strength and deformation parameters is less than 5.95. The micro-parameters determined by numerical simulation are shown in Tab. 2, including the micro-parameters of spherical particles and PBM.

2.3 Heating process and simulation scheme

Figs. 4 and 5 show the heat treatment process and simulation scheme of the TTSS model. From Fig. 4, the initial temperature of the TTSS model is set to20 °C, the surrounding boundary of the numerical model is used as the heat source, and the target temperature is 300 °C. Due to the temperature difference, the heat flows from all four sides of the numerical model to the center. The heating rate is set at5 °C/min. After reaching the target temperature (300 °C), the temperature remains constant until no thermally induced microcracks are generated. Finally, the numerical simulations are conducted on the TTSS model under different loading paths.

Fig. 5a shows the simulation scheme of the TTSS model under triaxial compression. The simulation scheme is divided into two stages, as follows:

(1) In the $0 \rightarrow t_1$ stage, the confining pressure is applied up to a certain value (5MPa, 15MPa, or 25MPa), the loading rate of the confining pressure set at 0.5 MPa/min.

(2) The confining pressure remains constant, and the deviatoric stress is applied with an axial displacement loading rate of 0.01 mm/s until the TTSS model fails ($t_1 \rightarrow t_2$).

The simulation scheme of the TTSS model under triaxial multi-level cyclic loading is shown in Fig. 5b. The stress level is determined based on the numerical results under triaxial compression, as listed in Table 3.

(1) The confining pressure is applied in consistency with simulation scheme under triaxial compression.

(2) The deviatoric stress path is a dynamic loading process with a cosine wave of a frequency of 0.2 Hz. The first few stress levels involve 20 loading cycles, with the amplitude maintained at 10 MPa. At the final stress level, deviatoric stress is applied in the same simulation scheme as mentioned above until the TTSS model fails.

3 Model results

3.1 Stress-strain curves

The typical stress-strain and microcrack-strain curves of the numerical model of the TTSS under different confining pressures are shown in Fig. 6. In this work, the compaction strain is regarded as positive and the dilation strain as negative. The axial strain isε_1, and the lateral strain is ε_3. The volumetric strain (ε_v) is obtained by$\varepsilon_v = \varepsilon_1 + 2\varepsilon_3$. The deviatoric stress is $q = \sigma_1 - \sigma_3$. The results show that the strength and deformation capacity of the TTSS model are related to the confining pressure (Fig. 6 (a, c, and e)). The peak strength, as the maximum deviatoric stress during the simulation process, increases with the increase of confining pressure. Zhang et al. (Zhang et al., 2022a) divided the stress-strain curve into three stages: the linear elastic stage; stable and unstable crack propagation stages; post-peak stage. At the linear elastic stage, the deviatoric stress increases linearly

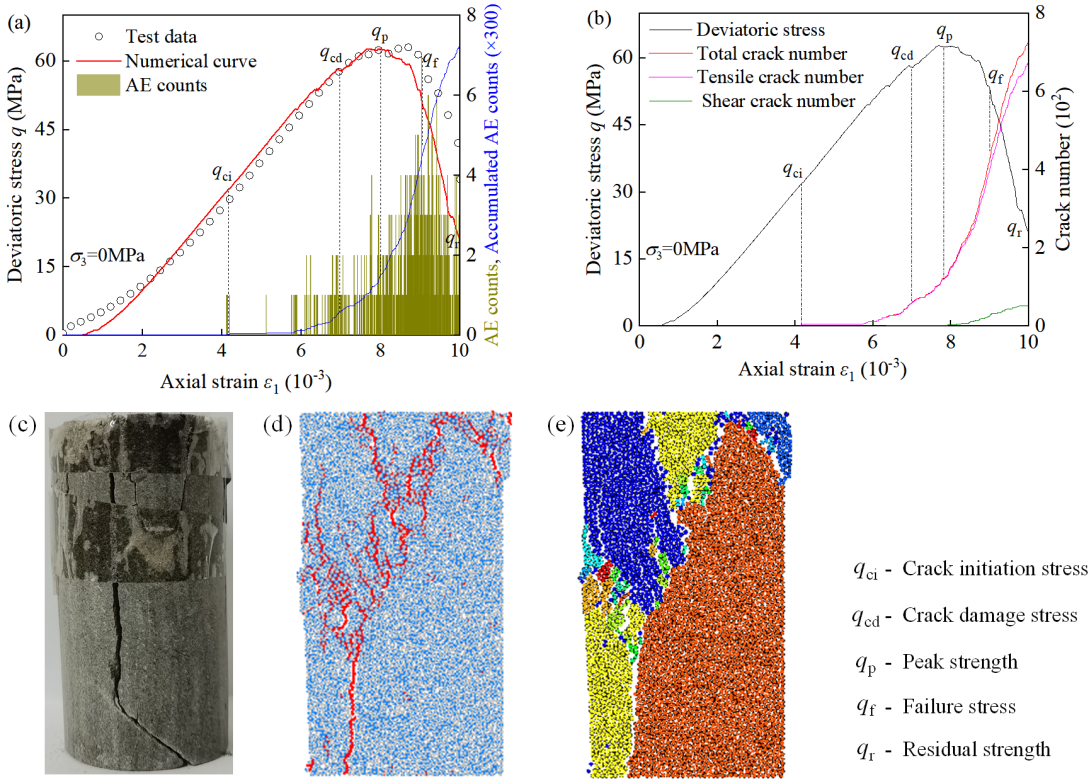

Fig. 3 Comparison the results of laboratory test and numerical simulation

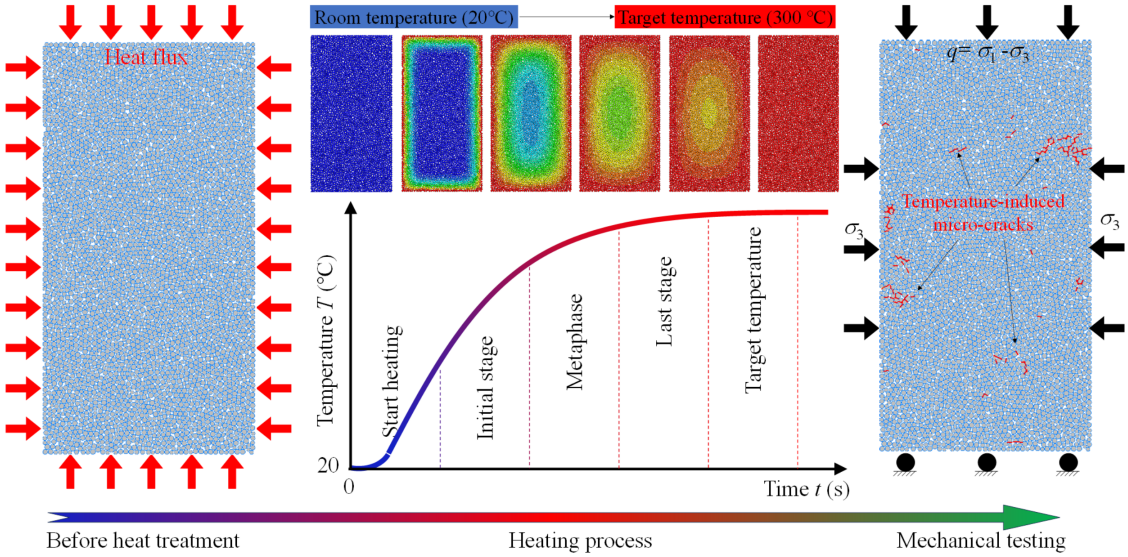

Fig. 4 Heating process

Tab. 1 Mechanical properties of sandstone

Mechanical properties	Experimental result	Numerical result	Deviation
Crack initiation stress (MPa)	29.78	32.05	2.27
Crack damage stress (MPa)	57.65	58.18	0.53
Peak strength (MPa)	62.40	62.98	0.58
Failure stress (MPa)	58.95	53.0	5.95
Elastic modulus (GPa)	9.35	10.43	1.08

Tab. 2 Micro-mechanical parameters of numerical model

Micro-parameters	Values
The minimum radius of the ball, R_{min} (mm)	0.02
Ratio of the maximum to the minimum radius of the ball, R_{rat}	1.5
Density of the ball, ρ (kg/m^3)	2700
Friction coefficient of the ball, μ	0.4
Friction angle of the parallel bond, φ (°)	40
Contact modulus of the parallel bond, E_c (GPa)	25
Ratio of normal to shear stiffness of the ball, k_n/k_s	4.0
Ratio of normal to shear stiffness of the parallel bond, k_n/k_s	1.25
Tensile strength of the parallel-bond σ_c (MPa)	45
Cohesion of the parallel-bond (MPa)	50
Initial radius multiplier of the parallel-bond	1.0

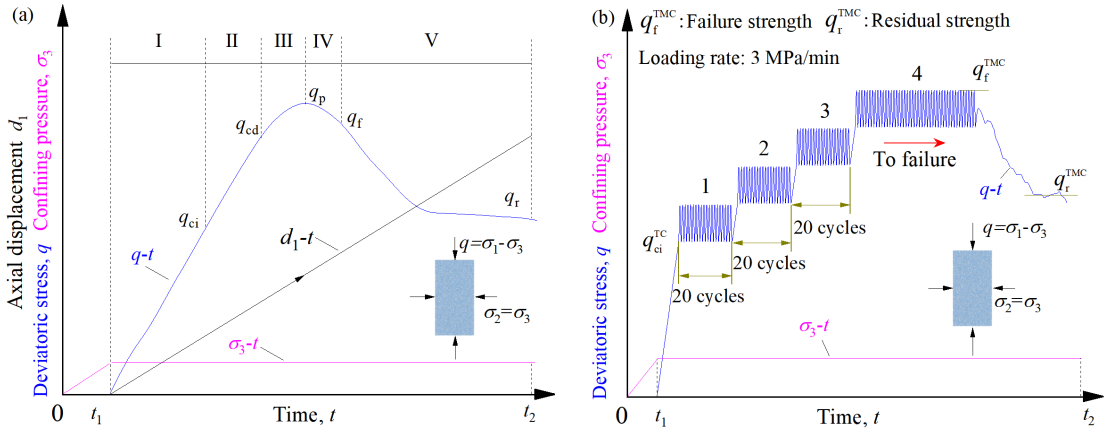

Fig. 5 Simulation schemes. (a) Monotonic loading; (b) Multi-level cyclic loading and unloading

Tab. 3 Applied stress limits to the TTSS model

Confining pressure (MPa)	Upper stress limit (MPa)	Lower stress limit (MPa)
5	45→55→65	35→45→55
15	50→60→70→80	40→50→60→70
25	53→63→73→83→93	43→53→63→73→83

with the increase of axial strain, and the deformation caused by compressive stress is restored after unloading. During the stable and unstable crack propagation stage, the slope of the deviatoric stress-lateral strain curve decreases. Finally, the deviatoric stress exceeds the bearing capacity and drops sharply in the post-peak stage, indicating that the increase rate of the plastic deformation is faster than the rate of recovery from elastic deformation. This is caused by the gradual development, coalescence, and interaction of local macrocracks.

The process of microcracks initiation, propagation, and connection in the TTSS model under triaxial compression is shown in Fig. 6 (b, d, and f). The microcracks are not formed in the initial stage (Stage I), indicating that almost all the energy input from the plane stress model is converted into elastic strain energy. When the stress reaches the crack initiation stress (Stage II), the bonding strength between particles is less than the shear stress or tensile stress, leading to bonding fracture. The microcracks present a disorderly distribution. As the stress gradually increases (Stage III), the distribution of microcracks gradually tends to be regular. When the stress exceeds the peak strength (Stage VI and V), the irreversible plastic deformation continues to increase, the microcracks gradually converge into macrocracks, and shear distribution zones are formed. When the shear distribution zones increase to a certain extent, the TTSS model fails.

Fig. 7 (a, c, and e) shows the stress-strain curves of the TTSS model under triaxial multi-level cyclic loading at different confining pressures. The loading and unloading curves do

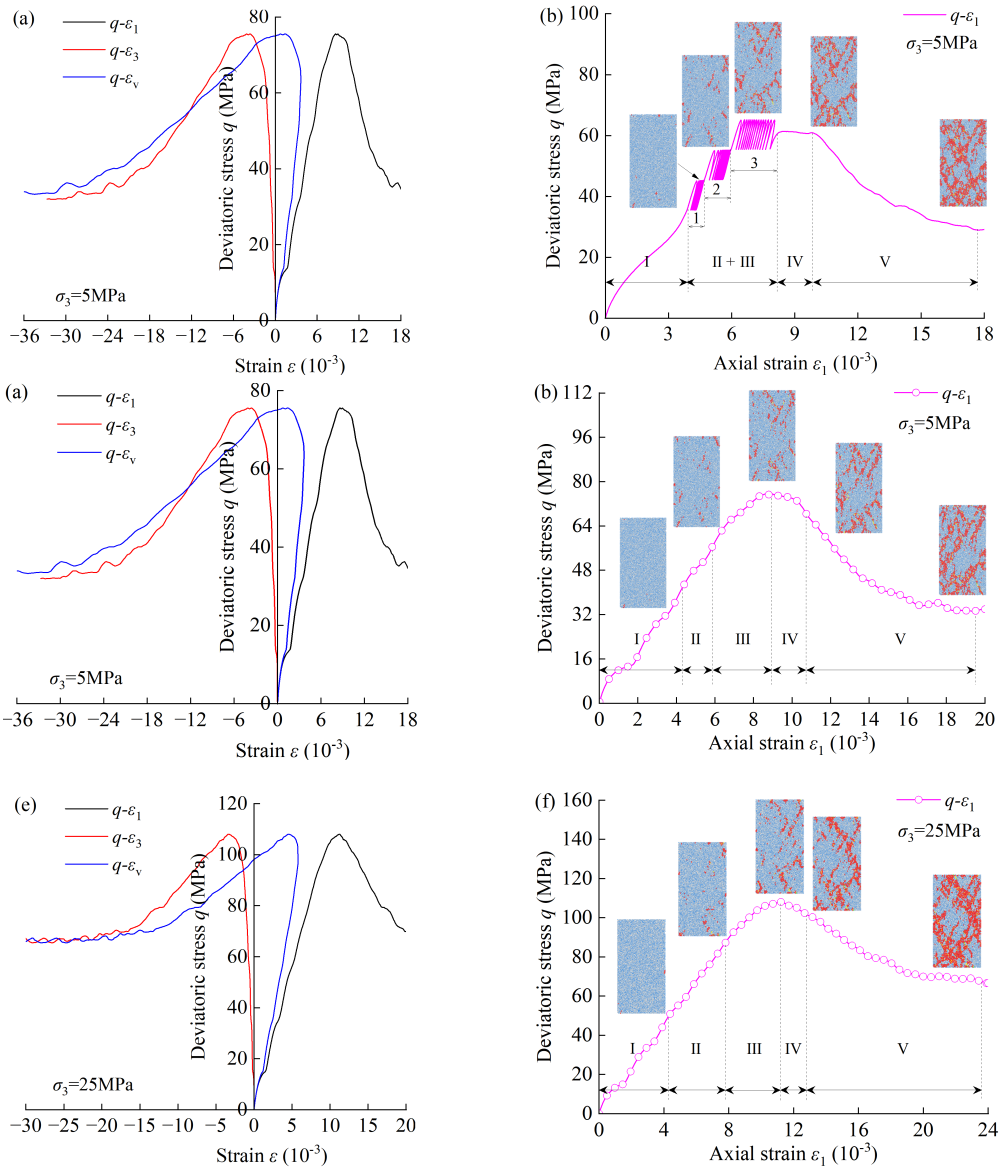

Fig. 6 Deviatoric stress-strain and microcrack-strain curves for the TTSS model under triaxial compression

not overlap, and hysteresis loop is formed during the loading and unloading. At low deviatoric stress levels, the density of the hysteresis curve changes from loose to dense. Due to the hardening caused by the compaction deformation of the TTSS model, the hysteresis loop becomes tighter. The irreversible plastic deformation gradually accumulates with the number of cycles, which is attributed to the development of the microcracks. At the final stress level, the hysteresis loop becomes sparser, and the hysteresis curve changes from loose to dense and then loose. This is due to the continuous opening and closing of the microcracks in the TTSS model during the cyclic loading, which aggravates the damage of the TTSS model. The increase in the number of loading cycles at the final stress level with the increase of confining pressure, indicating that the initiation, propagation, aggregation, and expansion of microcracks in the TTSS model are restricted by confining pressure.

The process of microcracks initiation, propagation, and connection in the TTSS model under triaxial multi-level cyclic loading is shown in Fig. 7 (b, d, and f). In the initial stage (Stage I), the microcracks are not formed, which is the same as the TTSS model under triaxial compression, indicating that almost all the energy input from the plane stress model is converted into elastic strain energy. When the deviatoric stress exceeds the first stress level (Stage II and III), the bonding strength between particles is less than the shear stress or tensile stress, leading to bonding fracture. The microcracks present a disorderly distribution. As the deviatoric stress level gradually increases, the distribution of the microcracks gradually tends to be regular. At the final stress level, the irreversible plastic deformation continues to increase, and the macrocracks are formed with the penetration of the microcracks. The density of the microcracks in the TTSS model increases with the increase of confining pressure, which is attributed to the TTSS model undergoes a greater number of loading cycles at the final stress level under

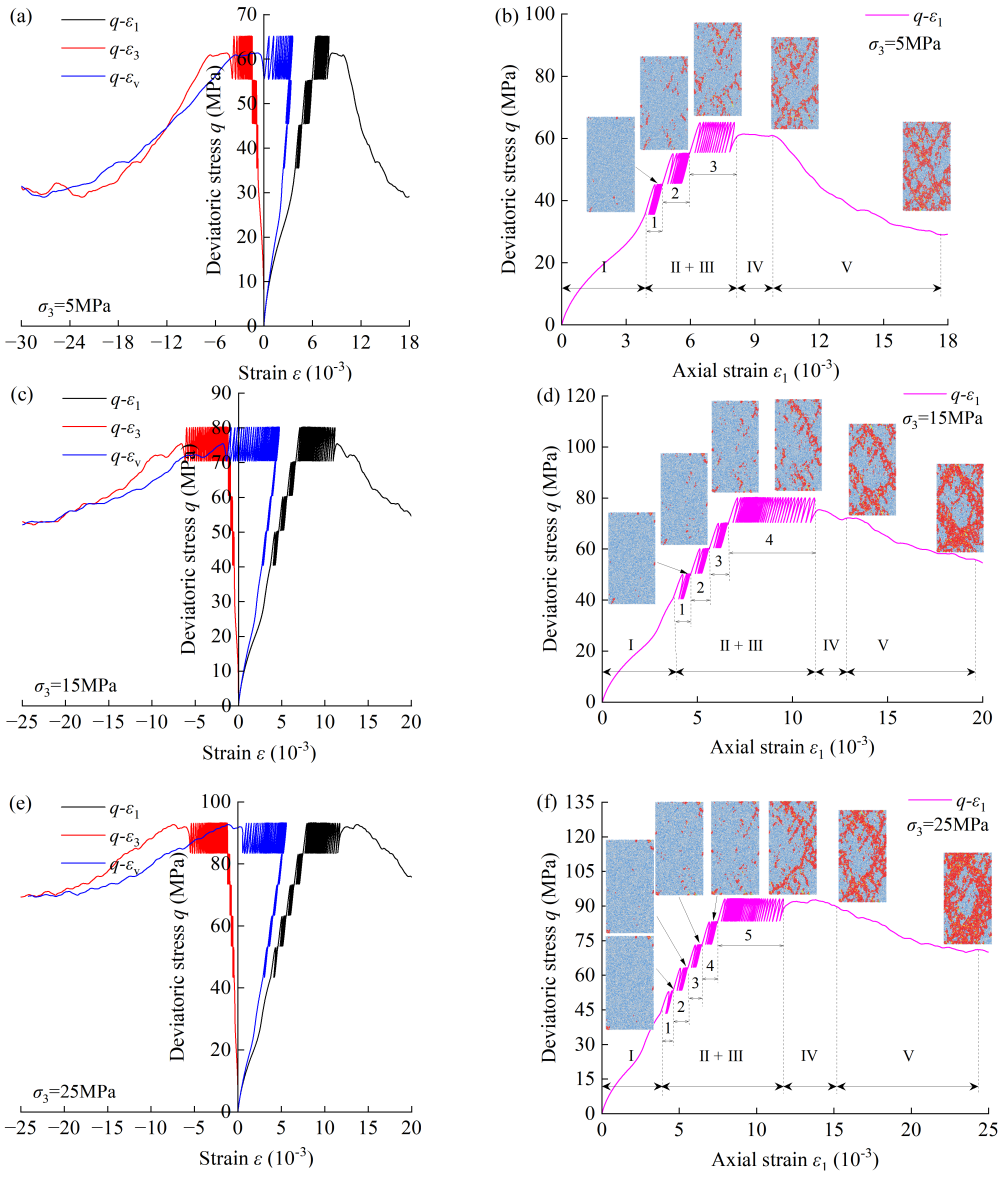

Fig. 7 Deviatoric stress-strain and microcrack-strain curves for the TTSS model under triaxial multi-level cyclic loading

high confining pressure. The fatigue effect decreases the failure strength of the TTSS model and increases the density of the microcracks.

3.2 Microcracks characteristics

Fig. 8 shows the relationship between the number of microcracks and axial strain of the TTSS model under triaxial compression and multi-level cyclic loading at different confining pressures. The evolution of the number of tensile and shear cracks at the microscale is presented. The green and purple lines respectively represent the number of tensile and shear cracks. The evolution of the number of the microcracks in the TTSS model under different confining pressures is similar. The proportion of tensile cracks gradually increases with the increase of the deformation of the TTSS model.

From Fig. 8 (a, c, and e), the curve of the number of microcracks with axial strain is relatively smooth. The initiation and propagation process of microcracks can be divided into three stages. In the elastic deformation stage, no microcracks form in the TTSS model. When the stress reaches the crack initiation stress, the number of the microcracks increases at an accelerating rate with the increase of deformation. When the axial strain exceeds the strain corresponding to the peak strength, the number of the microcracks increases at a decreasing rate with the increase of deformation. In the post-peak stage, the macrocracks are clearly visible.

From Fig. 8 (b, d, and f), the overall evolution of the number of microcracks in the TTSS model under triaxial multi-level cyclic loading is similar to that under triaxial compression, showing an increase first at an accelerating rate, then continues to increase at constant rate, and ultimately, increase at decreasing rate. The number of the microcracks exhibits a stepwise increase with increasing stress level. When the stress level is constant, the first few cycles make a significant contribution

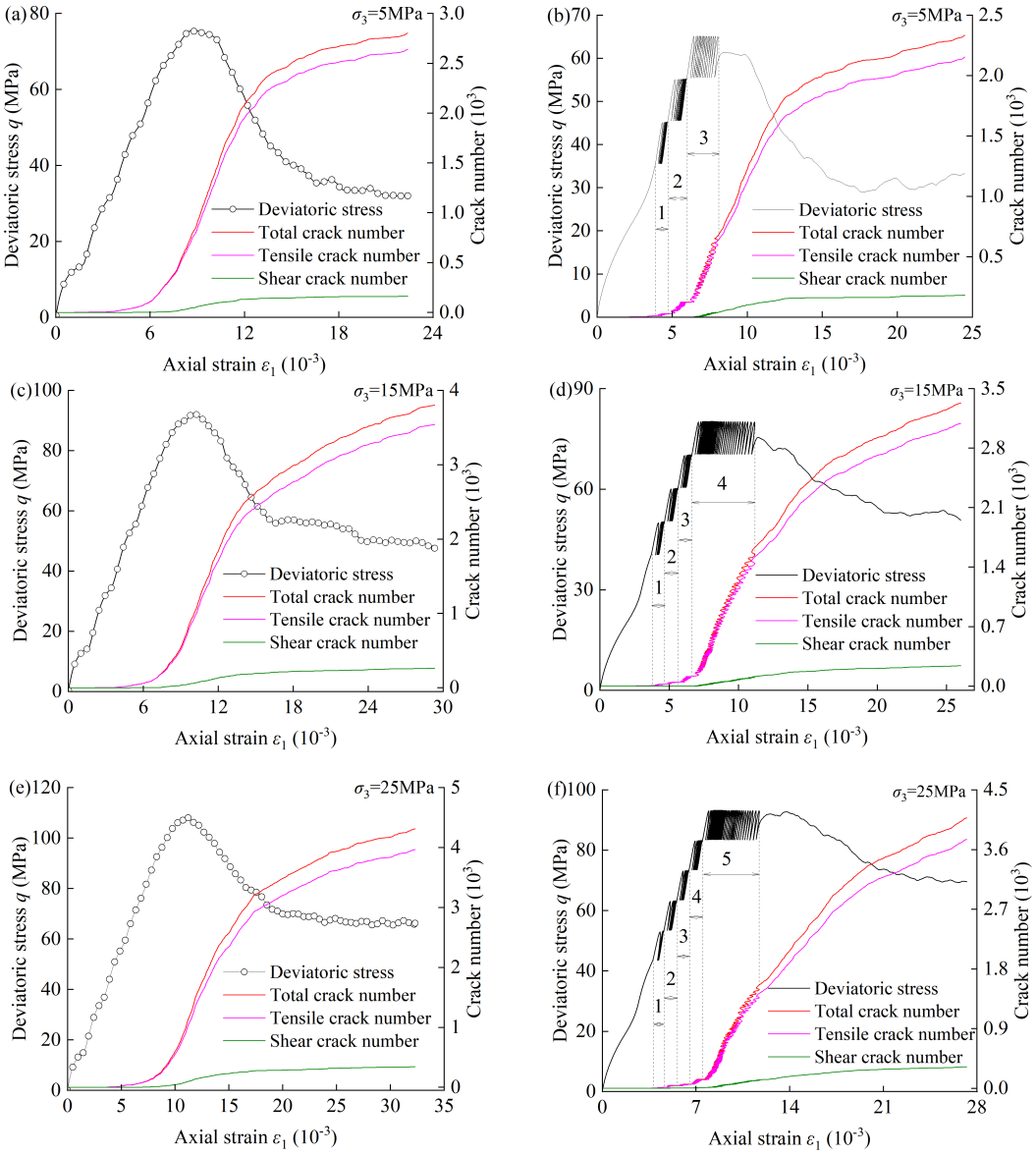

Fig. 8 Crack number of the TTSS model under triaxial monotonic and multi-level cyclic loading with different confining pressures

to the generation of the microcracks. The number of the microcracks increases during the loading stage, while decreases during unloading. This indicates that the microcracks open during loading and close during unloading. The cyclic loading increases the number of the microcracks in the TTSS model.

3.3 Energy evolution

Fig. 9 shows the evolution of the total strain energy, elastic energy, and dissipated energy of the TTSS model under triaxial monotonic and multi-level cyclic loading. The evolution of the TTSS model under different confining pressures is similar. Fig. 9 (a, c, and e) shows the evolution of the strain energy of the TTSS model under triaxial compression with different confining pressures. When the deviatoric stress is less than the crack initiation stress, the total strain energy and the elastic strain energy almost coincide, and the dissipated energy is almost zero, indicating that the energy absorbed by the TTSS model is converted into elastic energy stored in the TTSS model. The dissipated energy continues to increase with increasing deviatoric stress, while the increase rate of elastic strain energy decreases, indicating that the microcracks in the TTSS model initiate and propagate. In the unstable growth stage of microcracks, the ratio of dissipated strain energy to total strain energy gradually increases, which means that the growth rate of the microcracks in the TTSS model accelerates and the damage intensifies. The elastic strain energy is retained at a certain residual value in the post-peak stage, which is attributed to the lateral deformation of the TTSS model is constrained by confining pressure. The dissipated energy increases steadily after the stress reaches the peak strength, indicating that the microcracks still initiate, expand, and aggregate in the post-peak stage.

From Fig. 9 (b, d, and f) shows the evolution of the total

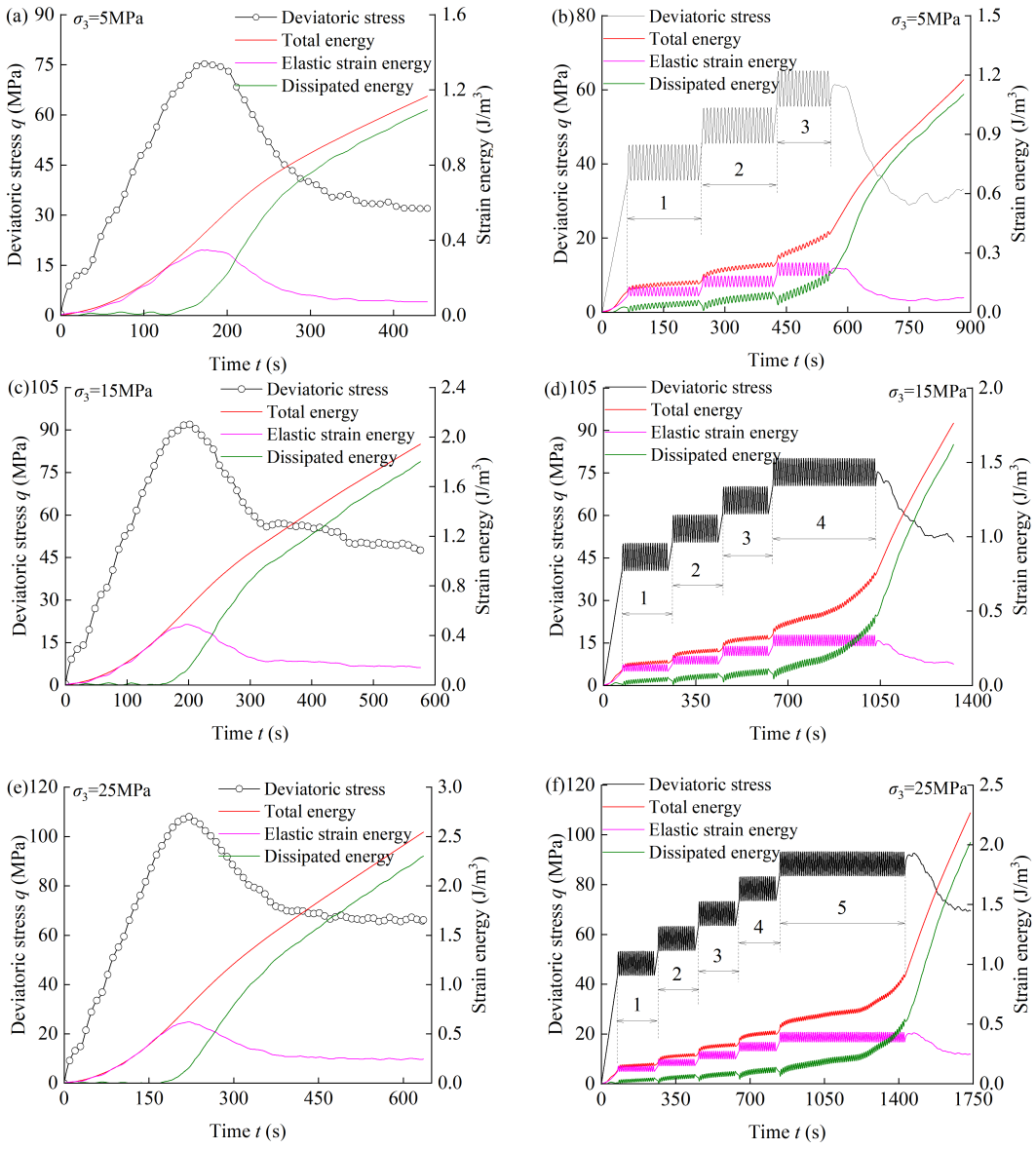

Fig. 9 Energy evolution of the TTSS model under triaxial monotonic and multi-level cyclic loading with different confining pressures

strain energy, elastic energy, and dissipated energy of the TTSS model under triaxial multi-level cyclic loading with different confining pressures. The total strain energy and dissipated energy increase exponentially, while the elastic strain energy first increases and then decreases. The total strain energy, dissipated energy, and elastic strain energy increase with increasing stress and decrease during unloading. The evolution of the strain energy of the TTSS model mainly depends on the stress level, fatigue effect, and confining pressure. The strain energy increase with increasing stress level. The strain energy generated during the first loading cycle under any constant stress level is the most pronounced. Strain energy increases with the number of cycles.

3.4 AE behavior

Acoustic emission monitoring technology is of great significance for exploring the damage accumulation, failure process, and crack evolution mechanism of internal microcracks in rock materials (Li et al. 2025). A series of studies are conducted on the AE counts and accumulated AE counts of the TTSS model under triaxial compression and multi-level cyclic loadings with different confining pressures. Fig. 10 shows the deviatoric stress-time curves, AE counts, and accumulated AE counts of the TTSS model under different confining pressures. The red histogram represents the evolution of AE counts with loading time, and the black and blue lines respectively represent deviatoric stress and accumulated AE counts. The results show that the AE characteristics of the TTSS model depend on the confining pressure and fatigue effect. The AE counts have both similarities and differences under triaxial monotonic and multi-level cyclic loading. These differences are mainly attributed to the variations in microcracks initiation and propagation patterns

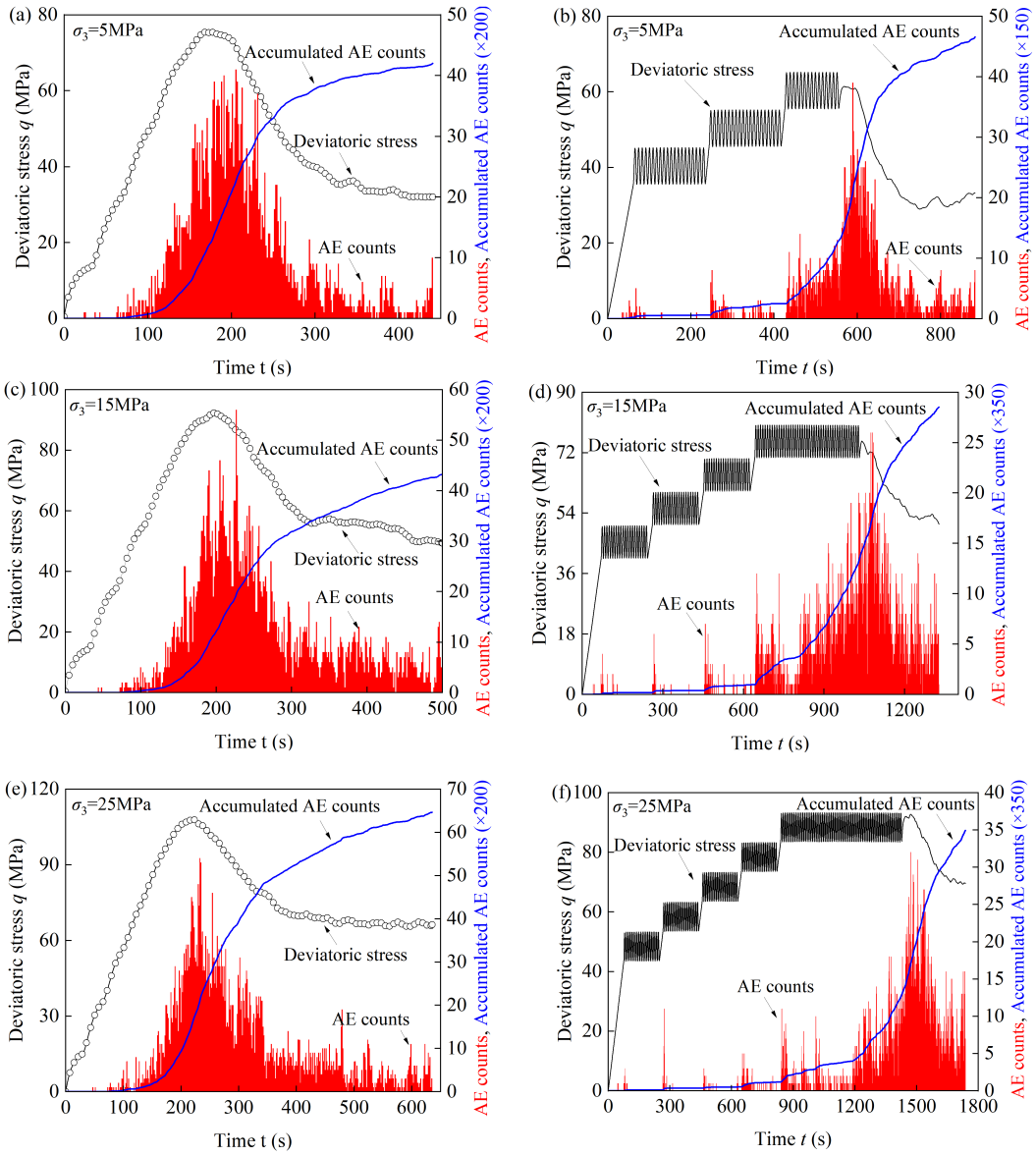

Fig. 10 AE behavior of the TTSS model under triaxial monotonic and multi-level cyclic loading with different confining pressures

in the TTSS model.

From Fig. 10 (a, c, and e), the deviatoric stress-time curves, AE counts, and accumulated AE counts of the TTSS model under triaxial monotonic with different confining pressures can be divided into the quiet period and active period. Since the quiet period corresponds to the elastic deformation stage, the deviatoric stress fluctuates slightly with loading time. The AE events are not very active, and the AE counts are also very small. This is because the internal microstructure of the TTSS model is gradually adjusted with increasing deviatoric stress. The AE counts enter the active period after the quiet period ends. During the active period, the stress-strain curve of the TTSS model undergo the stable and unstable growth of the microcracks. The accumulated AE counts do not increase steadily with loading time. The AE counts correspond to the initiation, propagation, and coalescence of the macrocracks in the TTSS model during the active period. The characteristic stress of the TTSS model under triaxial compression, including crack initiation stress, crack damage stress, peak strength, failure strength, and residual strength, can also be identified through the evolution of the AE counts (Zhang et al. 2022b). When the deviatoric stress reaches peak strength, the accumulated AE counts increase at a decelerating rate with loading time. This indicates that the microstructure inside the TTSS model is readjusted and redistributed in the post-peak stage. The AE characteristics are closely related to the microcracks initiation, propagation, and condensation of the TTSS model. The results are consistent with those of Miao et al. (Miao et al., 2023)

Fig. 10 (b, d, and f) shows the deviatoric stress-time curves, AE counts, and accumulated AE counts of the TTSS model under the multi-level cyclic loading. At the first few loading levels, the distribution of AE events exhibits a typical Kaiser

effect. The AE events mainly occur in the first few cycles at lower stress levels. The Kaiser effect indicates that the microcracks propagation of the TTSS model is activated in the first few cycles. The propagation rate of the microcracks gradually decreases to a constant value in the subsequent cycle of loading. At the final stress level, the AE counts first decrease and then increase with the number of cycles. The AE counts decrease with loading time in the post-peak stage. When the stress level is constant, the accumulated AE counts increase rapidly in the first few cycles and then increase at a constant rate. The growth rate of the accumulated AE counts increases with increasing stress level. At the final stress level, the accumulated AE counts increase at an increasing rate with the number of cycles. The accumulated AE counts increase at a decreasing rate with loading time in the post-peak stage, which is similar to those under triaxial compression. The AE counts of the TTSS model under triaxial multi-level cyclic loading depending on the confining pressure. The AE count is the largest when the TTSS model fails, and it increases with increasing confining pressure.

4 Conclusions

In this research, based on the particle flow discrete element programme, the mechanical behavior, microcrack propagation, energy evolution, failure mode, and acoustic emission characteristics of temperature-treated storage sandstone (TTSS) specimens were investigated through numerical simulation under triaxial compression and multi-level cyclic loading. The following conclusions can be drawn:

(1) Uniaxial compression test of sandstone at room temperature is performed. Based on the experimental results, the micro-parameters of the model in the particle flow program are confirmed. The stress-strain curve, peak strength, elastic modulus, and failure mode are put forward to determine the correctness and rationality of the numerical simulation method.

(2) The confining pressure has a significant influence on the mechanical behavior of the TTSS model, and the characteristic stress increases with increasing confining pressure. The fatigue effect reduces the failure strength of the TTSS model and increases the number and density of the microcracks.

(3) The evolution of the strain energy of the TTSS model mainly depends on the stress level, fatigue effect, and confining pressure. Strain energy, including the total strain energy, dissipated energy, and elastic strain energy, all increase with increasing stress level. The strain energy generated during the first loading cycle under any constant stress level is the most pronounced.

(4) The AE counts first increase and then decrease under triaxial compression. The AE events mainly occur in the first few cycles at lower stress levels. At the final stress level, the AE counts first decrease and then increase. The accumulated AE counts increase with increasing stress level.

Acknowledgements

This work was supported by the National Natural Science Foundation of China (42507223), Changsha Natural Science Foundation Project (kq2502062), Outstanding Youth Project of Hunan Provincial Department of Education (24B0294) are gratefully acknowledged. The authors would like to thank the anonymous referees for their valuable comments and suggestions.

Conflict of interest

The author declare no competing interest.

References

Aliyu MD, Archer RA 2021. A thermo-hydro-mechanical model of a hot dry rock geothermal reservoir. *Renewable Energy*, **176**: 475–493. doi:10.1016/j.renene.2021.05.070.

Bouman EA, Øberg MM, Hertwich EG 2016. Environmental impacts of balancing offshore wind power with compressed air energy storage (CAES). *Energy*, **95**: 91–98. doi:10.1016/j.energy.2015.11.041.

Cundall PA, Strack ODL 1979. A discrete numerical model for granular assemblies. *Géotechnique*, **29**(1): 47–65. doi:10.1680/geot.1979.29.1.47.

Damasceno DR, Spross J, Johansson F 2023. Rock mass response for lined rock caverns subjected to high internal gas pressure. *Journal of Rock Mechanics and Geotechnical Engineering*, **15**(1): 119–129. doi:10.1016/j.jrmge.2022.03.006.

Glamheden R, Curtis P 2006. Excavation of a cavern for high-pressure storage of natural gas. *Tunnelling and Underground Space Technology*, **21**(1): 56–67. doi:10.1016/j.tust.2005.06.002.

Glover PWJ, Baud P, Darot M, et al. 1995. α/β phase transition in quartz monitored using acoustic emissions. *Geophysical Journal International*, **120**: 775–782. doi:10.1111/j.1365-246X.1995.tb01852.x.

Guo PY, Bu MH, Zhang P, et al. 2023. Mechanical properties and crack propagation behavior of granite after high temperature treatment based on a thermo-mechanical grain-based model. *Rock Mechanics and Rock Engineering*, **56**(9): 6411–6435. doi:10.1007/s00603-023-03408-x.

Han ZC, Fan MM, Xu DB, et al. 2025. A study of stability and pericavity strain in an underground cavern group for compressed air energy storage. *GeoStorage*, **1**(1): 56–70. doi:10.46690/gs.2025.01.04.

Jiang ZM, Li P, Tang D, et al. 2020. Experimental and numerical investigations of small-scale lined rock cavern at shallow depth for compressed air energy storage. *Rock Mechanics and Rock Engineering*, **53**(6): 2671–2683. doi:10.1007/s00603-019-02009-x.

Kim HM, Park D, Ryu DW, et al. 2012a. Parametric sensitivity analysis of ground uplift above pressurized underground rock caverns. *Engineering Geology*, **135–136**: 60–65. doi:10.1016/j.enggeo.2012.03.006.

Kim HM, Rutqvist J, Ryu DW, et al. 2012b. Exploring the concept of compressed air energy storage (CAES) in lined rock caverns at shallow depth: A modeling study of air tightness and energy balance. *Applied Energy*, **92**: 653–667. doi:10.1016/j.apenergy.2011.07.013.

Kushnir R, Dayan A, Ullmann A 2012. Temperature and pressure variations within compressed air energy storage caverns. *International Journal of Heat and Mass Transfer*, **55**(21–22): 5616–5630. doi:10.1016/j.ijheatmasstransfer.2012.05.055.

Li BL, Sun T, Zhang JZ, et al. 2025. Experimental investigations on the strength, acoustic emission and failure characteristics of thermally cycled flawed granite under biaxial com-

pression. *International Journal of Thermal Sciences*, **215**: 110012. doi:10.1016/j.ijthermalsci.2025.110012.

Liu JJ, Yang CH, Song R, et al. 2025. Advances of geological storage engineering and technology. *GeoStorage*, **1**(1): 1–26. doi:10.46690/gs.2025.01.01.

Meng QB, Zhang MW, Han LJ, et al. 2018. Experimental research on the influence of loading rate on the mechanical properties of limestone in a high-temperature state. *Bulletin of Engineering Geology and the Environment*, **78**(5): 3479–3492. doi:10.1007/s10064-018-1332-4.

Miao ST, Pan PZ, Wang ZF, et al. 2023. Mechanism interpretation of sub-critical crack growth in Beishan granite subjected to cyclic loading. *Rock Mechanics and Rock Engineering*, **56**(11): 7777–7794. doi:10.1007/s00603-023-03467-0.

Perazzelli P, Anagnostou G 2017. Upper bound limit analysis of uplift failure in pressurized sealed rock tunnels. *International Journal for Numerical and Analytical Methods in Geomechanics*, **42**(5): 719–735. doi:10.1002/nag.2759.

Qin S, Xia C, Zhou S 2023. Air tightness of compressed air storage energy caverns with polymer sealing layer subjected to various air pressures. *Journal of Rock Mechanics and Geotechnical Engineering*, **15**(8): 2105–2116. doi:10.1016/j.jrmge.2022.10.007.

Rutqvist J, Kim HM, Ryu DW, et al. 2012. Modeling of coupled thermodynamic and geomechanical performance of underground compressed air energy storage in lined rock caverns. *International Journal of Rock Mechanics and Mining Sciences*, **52**: 71–81. doi:10.1016/j.ijrmms.2012.02.010.

Schmidt F, Menéndez J, Konietzky H, et al. 2020. Converting closed mines into giant batteries: Effects of cyclic loading on the geomechanical performance of underground compressed air energy storage systems. *Journal of Energy Storage*, **32**: 101882. doi:10.1016/j.est.2020.101882.

Tian WL, Yang SQ, Huang YH 2017. Macro and micro mechanics behavior of granite after heat treatment by cluster model in particle flow code. *Acta Mechanica Sinica*, **34**(1): 175–186. doi:10.1007/s10409-017-0714-3.

Tian WL, Yang SQ, Huang YH, et al. 2019. Mechanical behavior of granite with different grain sizes after high-temperature treatment by particle flow simulation. *Rock Mechanics and Rock Engineering*, **53**(4): 1791–1807. doi:10.1007/s00603-019-02005-1.

Tunsakul J, Jongpradist P, Kongkitkul W, et al. 2013. Investigation of failure behavior of continuous rock mass around cavern under high internal pressure. *Tunnelling and Underground Space Technology*, **34**: 110–123. doi:10.1016/j.tust.2012.11.004.

Xia C, Zhou Y, Zhou S, et al. 2015. A simplified and unified analytical solution for temperature and pressure variations in compressed air energy storage caverns. *Renewable Energy*, **74**: 718–726. doi:10.1016/j.renene.2014.08.058.

Xu C, Wang S, Xia C, et al. 2024a. Viscoelastic plastic interaction of tunnel support and strain-softening rock mass considering longitudinal effect. *Rock Mechancs Bulletin*, **3**(4): 100152. doi:10.1016/j.rockmb.2024.100152.

Xu C, Wang S, Xia CC 2024b. Analytical prediction for time-dependent interaction of a circular tunnel excavated in strain-softening rock mass. *Rock Mechanics Bulletin*, **3**(3): 100127. doi:10.1016/j.rockmb.2024.100127.

Yang X, Jiang ZM, Shi ZF, et al. 2025. Mechanical performance of polyurethane polymer mortar—A novel sealing material for CAES man-made caverns. *Journal of Energy Storage*, **106**: 114845. doi:10.1016/j.est.2024.114845.

Zareidarmiyan A, Salarirad H, Vilarrasa V, et al. 2020. Comparison of numerical codes for coupled thermo-hydro-mechanical simulations of fractured media. *Journal of Rock Mechanics and Geotechnical Engineering*, **12**(4): 850–865. doi:10.1016/j.jrmge.2019.12.016.

Zhang JZ, Long YD, Zhang T, et al. 2024. A true triaxial experiment investigation of the mechanical and deformation failure behaviors of flawed granite after exposure to high-temperature treatment. *Engineering Fracture Mechanics*, **306**: 110273. doi:10.1016/j.engfracmech.2024.110273.

Zhang T, Xu W, Wang H, et al. 2022a. Anisotropic mechanical characteristics and energy evolution of artificial columnar jointed rock masses subjected to multi-level cyclic loading. *International Journal of Fatigue*, **165**: 107215. doi:10.1016/j.ijfatigue.2022.107215.

Zhang T, Xu WY, Xu JR 2022b. Experimental and numerical investigations on the mechanical behavior of basalt in the dam foundation of the Baihetan Hydropower Station. *International Journal of Geomechanics*, **22**(2): 04021272. doi:10.1061/(ASCE)GM.1943-5622.0002267.

Zheng Z, Wang G, Yang C, et al. 2024. A novel nano-grade organosilicon polymer: Improving airtightness of compressed air energy storage in hard rock formations. *International Journal of Mining Science and Technology*, **34**(3): 305–321. doi:10.1016/j.ijmst.2024.02.003.

Zhou T, Zhang YY, Fan YL, et al. 2024. Effect of high-temperature and strain rate on the mechanical and cracking behaviors of flawed sandstone under dynamic impact loading. *Theoretical and Applied Fracture Mechanics*, **131**: 104405. doi:10.1016/j.tafmec.2024.104405.